ACS Catalysis
Letter
pubs.acs.org/acscatalysis

Cobalt Oxide Electrode Doped with Iridium Oxide as Highly Efficient Water Oxidation Electrode

Eunju Lee Tae,[†] Jihye Song,[†] A Reum Lee,[†] Caroline Hewon Kim,[†] Seokjun Yoon,[†] In Chul Hwang,[†] Min Gyu Kim,[‡] and Kyung Byung Yoon*[,†]

[†]Department of Chemistry, Sogang University, Seoul 04107, Korea

[‡]Pohang Accelerator Laboratory (PAL), Pohang University of Science and Technology, Pohang, Gyeongbuk 790-784, Korea

Supporting Information

ABSTRACT: Crystalline cobalt oxide nanoparticles (nc-CoO_x) supported on ITO glass or Ni foam doped with 5 mol % crystalline iridium oxide nanoparticles (nc-IrO_x) showed performances which are higher than those of nc-CoO_x on ITO or Ni foam and nc-IrO_x on a rotating glassy carbon disc electrode or Ni foam. The initial Co^{III} and Ir^{IV} become Co^{IV} and Ir^{VI} upon applying positive potentials. The nc-CoO_x particles intrinsically carry $Co^{III}O_5$ centers which become $Co^{IV}O_6$ centers upon application of positive potentials. The O vacancy in $Co^{III}O_5$ is transferred to $Ir^{VI}O_6$ upon application of positive potentials, giving rise to the formation of $Ir^{VI}O_5$ centers, which are proposed to be the highly active catalytic centers for water oxidation.

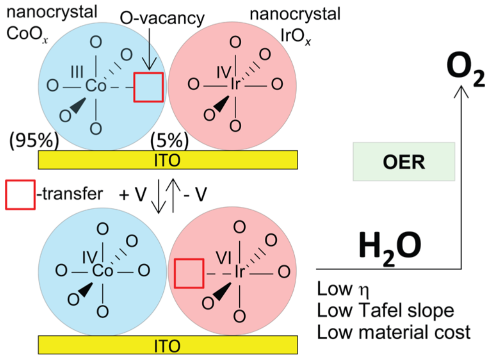

KEYWORDS: *water oxidation, crystalline cobalt oxide, crystalline iridium oxide, Tafel plot, XAS, EXAFS, oxygen vacancy*

Solar-electricity-driven water electrolysis is receiving great attention as a means to mitigate the rapid climate change caused by the severe use of fossil fuels.[1] For this method to be practically used in industry, the electrode performances should be enhanced (in particular, those of anodes). The three key factors to evaluate the anode performances are overpotenital (η) or the η value to obtain the current density (C_d) of 1 mA per cm^2 (η@1 mA cm^{-2}), Tafel slope (the amount of potential required to increase the reaction rate by a decade), and stability. To enhance anode performance, η and Tafel slope should be lowered, and stability should be increased.

As for anode materials with low η values, crystalline RuO_2[2] and iridium oxide nanocrystals (nc-IrO_x)[1d,3] have received great attention. The reported η@1 $mAcm^{-2}$ values of RuO_2-coated and nc-IrO_x-coated electrodes have been 0.2−0.3 V.[1d,2,3] However, both RuO_2 and nc-IrO_x electrodes have stability issues.[1d,4] Furthermore, from the view of the material costs, they are expensive. In this regard, cobalt oxide nanoparticles have received great attention.[1d,5,6] However, its reported η@1 $mAcm^{-2}$ value (>0.40 V) and Tafel slope (60 mV dec^{-1})[6] are much higher than those of nc-IrO_x electrode (0.2−0.25 V and 40 mV dec^{-1}, respectively),[3] indicating that the development of stable anodes with much lower η@1 $mAcm^{-2}$ values, Tafel slopes, and viable material costs has to be pursued.

We now report that the nc-CoO_x electrode doped with ∼5 mol % nc-IrO_x shows a much higher performance (η@1 $mAcm^{-2}$ < 0.2 V, Tafel slope = ∼ 30 mV dec^{-1}) than that of not only nc-CoO_x electrode but also that of the nc-IrO_x electrode (Figures S1 and S2). We also report that nc-CoO_x nanoparticles intrinsically carry penta-coordinated CoO_5 centers and the oxygen vacancy in CoO_5 is transferred to the doped nc-IrO_x nanoparticles, giving rise to the formation of catalytically active penta-coordinated $Ir^{VI}O_5$ centers during the oxygen evolution reaction (OER).

The nc-CoO_x deposited ITO glass electrodes ([nc-CoO_x]$_{ITO}$)[6] and the aqueous solution dispersed with nc-IrO_x nanoparticles[7] were prepared according to the literature procedures. The nc-IrO_x-doped nc-CoO_x/ITO electrodes ([nc-IrO_x/nc-CoO_x]$_{ITO}$) were prepared according to the procedure described in the Supporting Information. The top and side views of the scanning electron microscope (SEM) images of an [nc-IrO_x/nc-CoO_x]$_{ITO}$ electrode are shown in Figure 1a and 1b. Analyses showed that the loaded amount of nc-IrO_x nanoparticles gradually decreased from the top to the

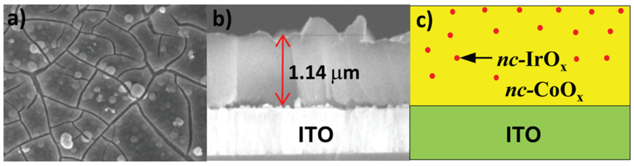

Figure 1. SEM images of [nc-IrO_x/nc-CoO_x]$_{ITO}$: (a) top and b) side views. (c) Illustration of the concentration profile of nc-IrO_x within the [nc-CoO_x]$_{ITO}$ film.

Received: May 11, 2015
Revised: August 14, 2015
Published: August 14, 2015

bottom as illustrated in Figure 1c (Figure S3). The total amount of nc-IrO_x within nc-CoO_x was 5 mol %. The calculated coverage (Γ_{Ir}) was 7.9×10^{-8} mol cm^{-2}. The nc-IrO_x-deposited ITO glass electrodes could not be prepared because the nc-IrO_x film was very readily detached from the ITO glass plate.

The cyclic voltamograms of $[nc\text{-}CoO_x]_{ITO}$ and $[nc\text{-}IrO_x/nc\text{-}CoO_x]_{ITO}$ at pH = 7 and 13.9 under the 0.1 M phosphate buffer solution and 1 M NaOH solution are shown in Figure 2a and 2b. The corresponding Tafel plots at pH 7 and 13.9 are shown in Figure 2c. Under the 0.1 M phosphate buffer solution, although the η@1 $mAcm^{-2}$ values of $[nc\text{-}CoO_x]_{ITO}$ were 0.37 (pH = 7) and 0.34 V (pH = 13), those of $[nc\text{-}IrO_x/nc\text{-}CoO_x]_{ITO}$ were 0.22 (pH = 7) and 0.19 V (pH = 13) (Table S1). All potentials are reported with respect to RHE unless specified otherwise. Thus, the doping of $[nc\text{-}CoO_x]_{ITO}$ with nc-IrO_x gives rise to a substantial decrease in η@1 $mAcm^{-2}$ (by 0.15 V), regardless of the pH. When compared with the reported η@1 $mAcm^{-2}$ values of $[nc\text{-}CoO_x]_{ITO}$ (0.4 V, at pH = 7) and nc-IrO_x-deposited rotating disc carbon electrode ($[nc\text{-}IrO_x]_{RDC}$) (0.20 V at pH = 7) and (0.22 V at pH = 13),[3] that of $[nc\text{-}CoO_x]_{ITO}$ prepared under our condition is a bit better than those prepared by other conditions,[6] and those of $[nc\text{-}IrO_x/nc\text{-}CoO_x]_{ITO}$ are similar or smaller than those of $[nc\text{-}IrO_x]_{ITO}$ (Table S1). Thus, from the view of η@1 $mAcm^{-2}$, the performance of $[nc\text{-}IrO_x/nc\text{-}CoO_x]_{ITO}$ is similar or superior to those of $[nc\text{-}IrO_x]_{RDC}$ electrodes despite the fact that $[nc\text{-}IrO_x/nc\text{-}CoO_x]_{ITO}$ contains only 5% of nc-IrO_x.

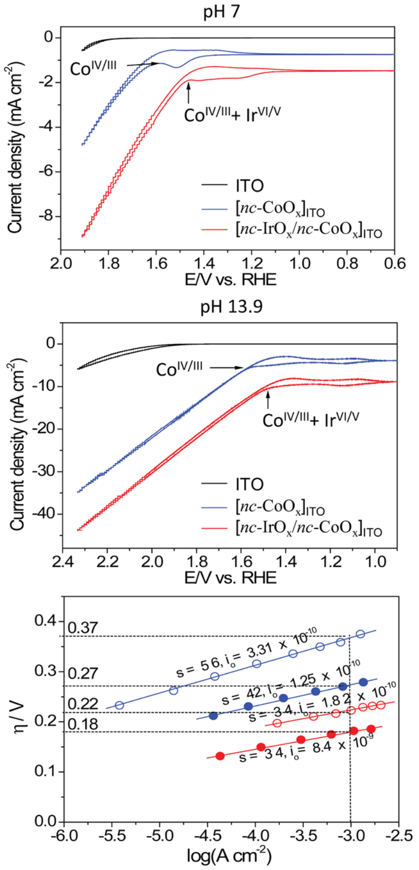

Figure 2. (a) and (b) Cyclic voltammograms of $[nc\text{-}CoO_x]_{ITO}$ and nc-IrO_x/nc-$CoO_x]_{ITO}$ electrodes in a pH 7 phosphate buffer (0.1 M) and pH 13.9 in 1 M NaOH solution. (c) Tafel plots, $\eta = V_{appl} - iR - E°$ where η is the overpotential, iR accounts for the uncompensated solution resistance, and $E°$ is the thermodynamic potential for water oxidation (open circle: pH 7, filled circle: pH 13.9).

The measured Tafel slopes of $[nc\text{-}IrO_x/nc\text{-}CoO_x]_{ITO}$ were 29–34 mV dec^{-1}, whereas those of $[nc\text{-}CoO_x]_{ITO}$ were 56–60 mV dec^{-1} (Table S1).[6] Thus, not only η@1 $mAcm^{-2}$ but also the Tafel slope significantly decreases (by 22–27 mV dec^{-1}) upon doping nc-IrO_x into $[nc\text{-}CoO_x]_{ITO}$. The Tafel slope of $[nc\text{-}IrO_x/nc\text{-}CoO_x]_{ITO}$ is even smaller than those of $[nc\text{-}IrO_x]_{RDC}$ (38–44 mV dec^{-1}) (Table S1).[3a]

The calculated TOF values of $[nc\text{-}CoO_x]_{ITO}$ per Co center and $[nc\text{-}IrO_x/nc\text{-}CoO_x]_{ITO}$ per Ir center at 1.913 V at pH = 7 are 0.19 and 19 s^{-1}, respectively (Table S1, Figure S4).[8] Thus, the TOF increases by 100 times upon doping $[nc\text{-}CoO_x]_{ITO}$ with nc-IrO_x nanoparticles, indicating that the nc-IrO_x doping gives rise to a dramatic increase (by 2 orders of magnitude) in the OER rate. Because the reported TOF values of $[nc\text{-}IrO_x]_{RDC}$ are ∼6–8 s^{-1}, the doping also gives rise to the increase in TOF by 2–3 times with respect to those of $[nc\text{-}IrO_x]_{RDC}$.

We also prepared Ni foam (Nif) electrodes deposited with nc-CoO_x ($[nc\text{-}CoO_x]_{Nif}$), nc-IrO_x ($[nc\text{-}IrO_x]_{Nif}$), and nc-IrO_x-doped nc-CoO_x ($[nc\text{-}IrO_x/nc\text{-}CoO_x]_{Nif}$) and compared their cyclic voltammograms (Figure 3a). We also compared their overpotential values at C_d = 10 mA cm^{-2} (η@10 mA cm^{-2}) at a time of 0 and 2 h, respectively, with those of various metal oxide deposited on rotating glass carbon (RDC) electrodes (Figure 3b). The η@10 mA cm^{-2} values of Nif, $[nc\text{-}CoO_x]_{Nif}$,

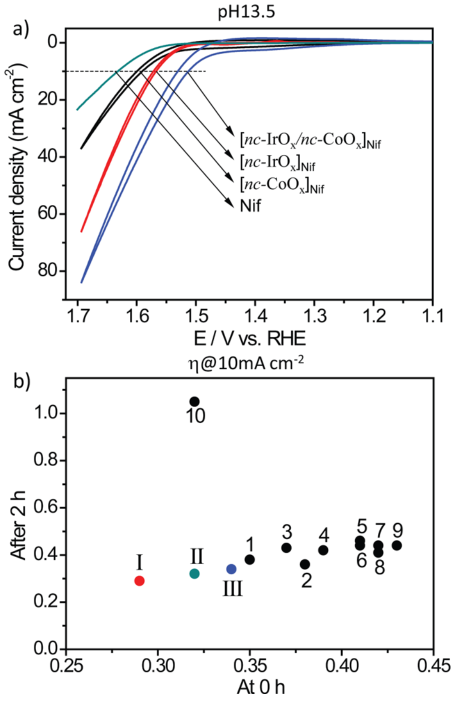

Figure 3. (a) Cyclic voltamograms of NiF, $[nc\text{-}CoO_x]_{Nif}$, $[nc\text{-}IrO_x]_{Nif}$, and $[nc\text{-}IrO_x/nc\text{-}CoO_x]_{Nif}$ at pH = 13.5 with the scan rate of 5 mV s^{-1}. (b) The plots of η@10 mA cm^{-2} values of $[nc\text{-}CoO_x]_{Nif}$ (III), $[nc\text{-}IrO_x]_{Nif}$ (II), and $[nc\text{-}IrO_x/nc\text{-}CoO_x]_{Nif}$ (I), and various metal oxide materials deposited on RDC at time = 0 (x-axis) and 2 h (y-axis). The numbered data points were borrowed from ref 1d. 1: $[NiFeO_x]_{RDC}$, 2: $[NiCoO_x]_{RDC}$, 3: $[CoFeO_x]_{RDC}$, 4: $[nc\text{-}CoO_x\text{-}a]_{RDC}$, 5: $[NiLaO_x]_{RDC}$, 6: $[NiCuO_x]_{RDC}$, 7: $[NiO_x]_{RDC}$, 8: $[nc\text{-}CoO_x\text{-}b]_{RDC}$, 9: $[NiCeO_x]_{RDC}$, 10: $[nc\text{-}IrO_x]_{RDC}$.

$[\text{nc-IrO}_x]_{\text{Nif}}$, and $[\text{nc-IrO}_x/\text{nc-CoO}_x]_{\text{Nif}}$ were 0.39, 0.36, 0.33, and 0.28 V, respectively (Figure 3a). As can be seen from Figure 3b, the η@10 mA cm^{-2} value of $[\text{nc-IrO}_x/\text{nc-CoO}_x]_{\text{Nif}}$) was the lowest. Furthermore, unlike $[\text{nc-IrO}_x]_{\text{RDC}}$, $[\text{nc-IrO}_x/\text{nc-CoO}_x]_{\text{Nif}}$ is quite stable, as shown in Figure 3b. The calculated relative roughness factors of Ni plate, $[\text{nc-CoO}_x]_{\text{Nif}}$, $[\text{nc-IrO}_x]_{\text{Nif}}$, and $[\text{nc-IrO}_x/\text{nc-CoO}_x]_{\text{Nif}}$ were 1, 12, 8, and 100, respectively (Table S2, Figure S5). Thus, the roughness factor $[\text{nc-IrO}_x/\text{nc-CoO}_x]_{\text{Nif}}$ is about 10 times higher than that of $[\text{nc-CoO}_x]_{\text{Nif}}$ and $[\text{nc-IrO}_x]_{\text{Nif}}$.

The Tafel plots of $[\text{nc-IrO}_x/\text{nc-CoO}_x]_{\text{ITO}}$ measured in the 1 M phosphate buffer solutions with different pH values between 4.54 and 13.9 are shown in Figure 4a. The measured Tafel slopes of $[\text{nc-IrO}_x/\text{nc-CoO}_x]_{\text{ITO}}$ were between 25.9 and 34 mV dec^{-1} (average = 31.4 mV dec^{-1}). The plot of $\ln C_d$ versus pH at a constant potential (0.75 V vs Ag/AgCl) shows that the slope is nearly 2 (1.99) (Figure 4b).

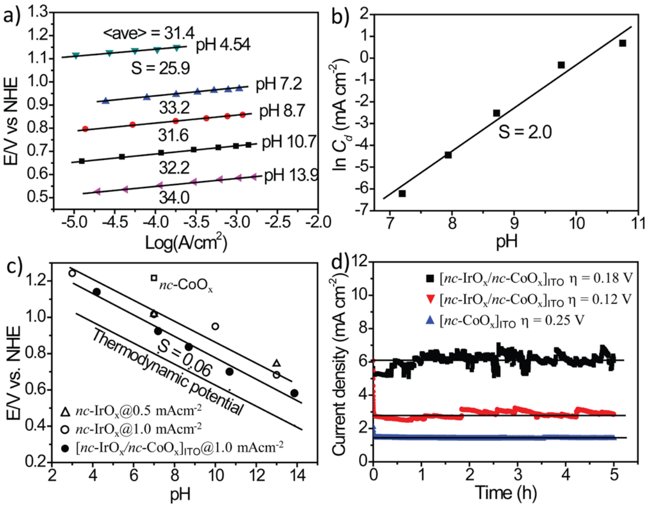

Figure 4. (a) Tafel plots of $[\text{nc-IrO}_x/\text{nc-CoO}_x]_{\text{ITO}}$ corrected for the series resistance ($\eta = V_{\text{appl}} - iR - E^{\circ}$) prepared by the corresponding 1 M phosphate buffer and 1 M NaOH solution for pH = 13.9. (b) The plot of $\ln C_d$ with respect to pH for $[\text{nc-IrO}_x/\text{nc-CoO}_x]_{\text{ITO}}$ at 0.75 V versus Ag/AgCl in the corresponding phosphate buffer. (c) The plot of η@1 mAcm^{-2} with respect to pH (open square, open triangle, and open circle represent the corresponding values of $[\text{nc-IrO}_x]_{\text{RDC}}$ borrowed from ref 6, ref 3b, and ref 3a, respectively). (d) The plots of C_d with respect to time for $[\text{nc-CoO}_x]_{\text{ITO}}$ and $[\text{nc-IrO}_x/\text{nc-CoO}_x]_{\text{ITO}}$ at η of 0.18 V, 0.12, and 0.25 V at pH = 13.

Accordingly, the kinetic current (i_k) for OER at a low η region for $[\text{nc-IrO}_x/\text{nc-CoO}_x]_{\text{ITO}}$ can be expressed as in eq 1.[9]

$$i_k = nFAk(a_{H^+})^{-2}\exp\left(\frac{F\eta}{2RT}\right) \tag{1}$$

where, n is the number of electron, F is the Faraday constant, A is the area, k is the rate constant of the OER reaction, respectively.

The $(\delta V/\delta \text{pH})_i$ plot of $[\text{nc-IrO}_x/\text{nc-CoO}_x]_{\text{ITO}}$ at the potential which gives 1 mA cm^{-2} is shown in Figure 4c. The corresponding plots for the thermodynamic potential for OER and the data points of $[\text{nc-IrO}_x]_{\text{RDC}}$ from the literature are also shown. The plots again show that the η@1 mAcm^{-2} values of $[\text{nc-IrO}_x/\text{nc-CoO}_x]_{\text{ITO}}$ (0.2, 0.17, 0.14, 0.12, and 0.17 V at pH = 4.5, 7.2, 8.7, 10.7, and 13.9, respectively) are substantially smaller than 0.2 V (average = 0.16 V) under the 1 M electrolyte condition. The average η@1 mAcm^{-2} value is also smaller than those of $[\text{nc-IrO}_x]_{\text{RDC}}$.[3a,c]

We deduced eq 2 from the experimental observation that the slope is −0.06 V pH^{-1} (Figure 4c) and eq 3 from the experimental observation that the Tafel slope is nearly 30 (Figure 4a).

$$\left(\frac{\delta V}{\delta \text{pH}}\right)_i = -\left(\frac{RT}{F}\right) \tag{2}$$

$$\left(\frac{\delta V}{\delta \ln i}\right)_{\text{pH}} = \left(\frac{RT}{2F}\right) \tag{3}$$

To satisfy eqs 2 and 3, the number of electrons, n, in eq 1 was set to be 2 (eq 4).

$$i_k = 2FAk(a_{H^+})^{-2}\exp\left(\frac{F\eta}{2RT}\right) \tag{4}$$

Thus, we deduce that two-electron processes take place (in a concerted or a stepwise manner) before the rate-determining step (rds) of OER on $[\text{nc-IrO}_x/\text{nc-CoO}_x]_{\text{ITO}}$, and rds does not involve electron transfer. Figure 4d further shows the stability of $[\text{nc-IrO}_x/\text{nc-CoO}_x]_{\text{ITO}}$. Thus, C_d remains constant at 2.8 and 6.2 mA cm^{-2} for the tested 5 h period at η = 0.12 and 0.18 V, respectively, at pH 13. The Faraday efficiency is 100% (Figure S6). Note that C_d of $[\text{nc-CoO}_x]_{\text{ITO}}$ also remains constant but at 1.5 mA cm^{-2}. The fluctuation of C_d of $[\text{nc-IrO}_x/\text{nc-CoO}_x]_{\text{ITO}}$ (Figure 4d) occurs due to the vigorous formation of O_2 bubbles on the electrode surface.

To verify electronic and local geometric structural origin responsible for the electrochemical property, in situ Co K- and Ir L_{III}-edges X-ray absorption fine structure (XAFS) spectra for $[\text{nc-IrO}_x/\text{nc-CoO}_x]_{\text{ITO}}$ have been investigated at pH 13 under the applied potential of 1.97 V (Figure S7). The Co K- and Ir L_{III}-edges X-ray absorption near edge structure (XANES) spectra revealed that the initial averaged oxidation states of the Co ions are about III and Ir ions are IV in $[\text{nc-IrO}_x/\text{nc-CoO}_x]_{\text{ITO}}$ and Co$^{\text{III}}$ is oxidized to Co$^{\text{IV}}$ completely and Ir$^{\text{IV}}$ is effectively oxidized to Ir$^{\text{VI}}$ at 1.97 V upon this applied voltage.[10a−c]

The Fourier-transformed (FT) radial distribution functions (RDF) of Co K- and Ir L_{III}-edges extended X-ray absorption fine structure (EXAFS) spectra of $[\text{nc-CoO}_x]_{\text{ITO}}$ and $[\text{nc-IrO}_x/\text{nc-CoO}_x]_{\text{ITO}}$ are shown in Figure 5. With no applied potential (V_{oc}), the overall RDF peak features for Co ions in both $[\text{nc-CoO}_x]_{\text{ITO}}$ and $[\text{nc-IrO}_x/\text{nc-CoO}_x]_{\text{ITO}}$ are typically characteristic of the two-dimensional layered structure, in which each octahedral environment around Co$^{\text{IV}}$ ions is interlinked by sharing the edges (via di-μ_2-oxo bridging, Figure S8), consistent with the literature reports.[10a,d] The first FT peak is assigned to be arising from the Co−O bonding in the single octahedron, and the second peak corresponds to the Co−Co bond distance by way of di-μ_2-oxo bridged neighboring octahedra.

The overall RDF peak features for Ir ion in $[\text{nc-IrO}_x/\text{nc-CoO}_x]_{\text{ITO}}$ are also characteristic of the two-dimensional layered structure. Interestingly, however, an additional third FT peak at around ∼3.5 Å was observed from the Ir L_{III}-edge RDF, relevant to corner-shared IrO_6 octahedra (via mono-μ-oxo bridging). Therefore, it is concluded that the nc-IrO_x nanoparticles have the edge-shared octahedral site as the major phase and the corner-shared octahedral site as the minor or defected phase. Beller and the co-workers also observed the

DOI: 10.1021/acscatal.5b00979
ACS Catal. 2015, 5, 5525−5529

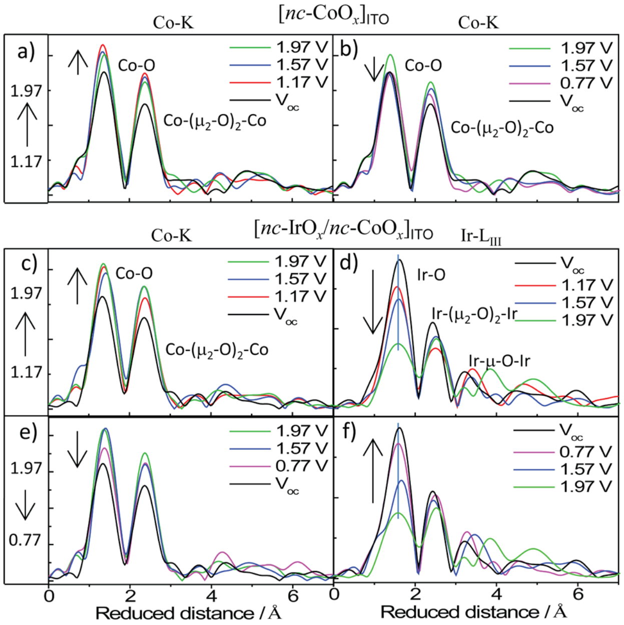

Figure 5. Fourier transforms of Co−K edge EXAFS spectra with (a) increasing and (b) decreasing applied potentials and those of Ir-L$_{III}$ edge EXAFS spectra for [nc-IrO$_x$/nc-CoO$_x$]$_{ITO}$ with (c), (d) increasing and (e), (f) decreasing applied potentials at pH = 13.

minor phase.[11] The calculated EXAFS structural parameters are summarized in Table S3 and S4.

Interestingly, upon applying an oxidative potential (1.17−1.97 V, η = −0.06−0.74 V), the FT peak intensity of Co−O bonding in [nc-CoO$_x$]$_{ITO}$ increases (Figure 5a) and, upon decreasing the positive potential or applying a slightly reductive potential (0.77 V), it decreases back to the initial intensity (Figure 5b).

Although the research groups of Nocera[10a] and Dau[10d] conducted X-ray absorption studies on [nc-CoO$_x$]$_{ITO}$, Nocera's group did not report RDF of Co K-edge EXAFS spectra and Dau's group did not report *in situ* X-ray absorption studies at various applied potentials.

Accordingly, to date, this important phenomenon has not been known. This phenomenon indicates that nc-CoO$_x$ intrinsically carries coordinatively unsaturated Co^{III}O$_5$ centers, which pick up O atoms from water to fill up the O vacancy (☐) upon applying the oxidative potential condition, and subsequently return back to Co^{III}O$_5$ states upon decreasing the oxidative potential (Scheme 1).

Scheme 1. Oxidative Potential Mediated Reversible Transformation of Co^{III}O$_5$ to Co^{IV}O$_6$ in nc-CoO$_x$

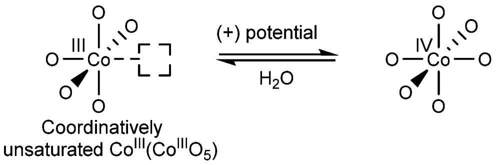

This seems to be origin of the benefit of the nonstoichiometric nanocrystalline cobalt oxide. Such an interesting phenomenon (Scheme 1) is unprecedented because such an interesting phenomenon has not been observed from IrO$_x$[12] and Co(OH)$_2$.[13] More interestingly, the O vacancy in Co^{III}O$_5$ is transferred to Ir^{VI}O$_6$ octahedra, upon applying oxidative potentials, despite the fact that the oxidation state of Ir is VI. Thus, while the FT peak intensity of Co−O bonding increases (Figure 5c) that of Ir−O bonding decreases (Figure 5d) upon applying oxidative potentials. Upon removing the oxidative potential, the intensity of the Co−O bonding partially decreases (Figure 5e) while that of Ir−O bonding increases almost back to the original peak intensity (Figure 5f).

This phenomenon indicates that the Co^{III}O$_5$ centers of nc-CoO$_x$ nanoparticles interfaced with nc-IrO$_x$ nanoparticles transfer the O vacancies to the Ir^{VI}O$_6$ centers upon application of oxidative potentials (Scheme 2). We propose that Ir^{VI}O$_5$ species are the active species which give rise to the outstanding performance of [nc-IrO$_x$/nc-CoO$_x$]$_{ITO}$ in OER. Further details about the proposed two-electron transfer mechanisms[14−16] are shown in Supporting Information.

Scheme 2. Oxygen Vacancy Transfer from Co^{III}O$_5$ to Ir^{VI}O$_5$ at the Interface

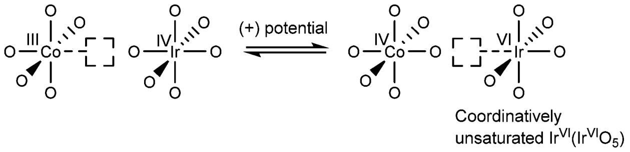

In summary, we report that the doping of nc-CoO$_x$ with 5% nc-IrO$_x$ nanoparticles leads to a very stable nc-IrO$_x$-doped nc-CoO$_x$ electrode whose performances in terms of η@1 mAcm^{-2}, η@10 mAcm^{-2}, and Tafel slope exceed those of not only nc-CoO$_x$ but also nc-IrO$_x$. In nc-IrO$_x$-doped nc-CoO$_x$ electrodes both nc-CoO$_x$ and nc-IrO$_x$ nanoparticles exist in the edge-shared two-dimensional layered structure. The nc-IrO$_x$ nanoparticles also have corner-shared IrO$_6$ octahedral defects. The nc-CoO$_x$ nanoparticles intrinsically carry coordinatively unsaturated Co^{III}O$_5$ centers, which becomes coordinatively saturated Co^{IV}O$_6$ centers by picking up an O atom from water when an oxidative potential (>1.17 V vs RHE) is applied. In cases of nc-IrO$_x$-doped nc-CoO$_x$ electrodes, the oxidation states of Ir are IV and Co are about III when no oxidative potential is applied. Upon applying an oxidative potential (>1.17 V) Ir^{IV} becomes Ir^{VI} and Co^{III} changes to Co^{IV}. Simultaneously, the transfer of the O vacancy takes place from Co^{III}O$_5$ centers to Ir^{VI}O$_6$ centers, leading to the formation of Ir^{VI}O$_5$ centers, which is assigned to be highly active catalytic centers for OER. Thus, nc-IrO$_x$-doped nc-CoO$_x$ electrodes are much more compelling than nc-IrO$_x$ electrodes in terms of the material cost and the performance. The calculated relative roughness factors of nc-CoO$_x$, nc-IrO$_x$, and nc-IrO$_x$-doped nc-CoO$_x$ electrodes were 1.0, 0.7, and 8.3, respectively.

■ ASSOCIATED CONTENT

Ⓢ Supporting Information

The Supporting Information is available free of charge on the ACS Publications website at DOI: 10.1021/acscatal.5b00979.

Details of the proposed two-electron mechanisms, experimental section, structural parameters obtained from EXAFS curve-fitting for the Co K-edge k^2-weighted EXAFS spectra of the [nc-CoO$_x$]$_{ITO}$ and [nc-IrO$_x$/nc-CoO$_x$]$_{ITO}$. The EDS elemental mapping images on the TEM of [nc-IrO$_x$/nc-CoO$_x$]$_{ITO}$XANE spectra of films and references (PDF)

AUTHOR INFORMATION

Corresponding Author

*E-mail: yoonkb@sogang.ac.kr. Phone: 82-02-715-2569. Fax: 82-02-706-4269.

Notes

The authors declare no competing financial interest.

ACKNOWLEDGMENTS

This work was supported by the Korea Center for Artificial Photosynthesis (KCAP), located at Sogang University and funded by the Ministry of Science, ICT and Future Planning through the National Research Foundation of Korea, No. 2009-0093886. We thank Jiyun Lee for the help in preparing the manuscript.

REFERENCES

(1) (a) Faunce, T. A.; Lubitz, W.; Rutherford, A. W. (Bill); MacFarlane, D.; Moore, G. F.; Yang, P.; Nocera, D. G.; Moore, T. A.; Gregory, D. H.; Fukuzumi, S.; Yoon, K. B.; Armstrong, F. A.; Wasielewski, M. R.; Styring, S. *Energy Environ. Sci.* **2013**, *6*, 695−698. (b) Cook, T. R.; Dogutan, D. K.; Reece, S. Y.; Surendranath, Y.; Teets, T. S.; Nocera, D. G. *Chem. Rev.* **2010**, *110*, 6474−6502. (c) Chen, Z.; Meyer, T. J. *Angew. Chem., Int. Ed.* **2013**, *52*, 700−703. (d) McCrory, C. C. L.; Jung, S.; Peters, J. C.; Jaramillo, T. F. *J. Am. Chem. Soc.* **2013**, *135*, 16977−16987.

(2) (a) Matsumoto, Y.; Sato, E. *Mater. Chem. Phys.* **1986**, *14*, 397−426. (b) Lyons, M. E. G.; Floquet, S. *Phys. Chem. Chem. Phys.* **2011**, *13*, 5314−5335. (c) Reier, T.; Oezaslan, M.; Strasser, P. *ACS Catal.* **2012**, *2*, 1765−1772.

(3) (a) Zhao, Y.; Vargas-Barbosa, N. M.; Hernandez-Pagan, E. A.; Mallouk, T. E. *Small* **2011**, *7*, 2087−2093. (b) Nakagawa, T.; Beasley, C. A.; Murray, R. W. *J. Phys. Chem. C* **2009**, *113*, 12958−12961. (c) Blakemore, J. D.; Schley, N. D.; Olack, G. W.; Incarvito, C. D.; Brudvig, G. W.; Crabtree, R. H. *Chem. Sci.* **2011**, *2*, 94−98.

(4) Hine, F.; Yasuda, M.; Noda, T.; Yoshida, T.; Okuda, J. *J. Electrochem. Soc.* **1979**, *126*, 1439−1445.

(5) (a) Doyle, R. L.; Godwin, I. J.; Brandon, M. P.; Lyons, M. E. G. *Phys. Chem. Chem. Phys.* **2013**, *15*, 13737−13783. (b) Jiao, F.; Frei, H. *Energy Environ. Sci.* **2010**, *3*, 1018−1027. (c) Artero, V.; Chavarot-Kerlidou, M.; Fontecave, M. *Angew. Chem., Int. Ed.* **2011**, *50*, 7238−7266. (d) Chou, N. H.; Ross, P. N.; Bell, A. T.; Tilley, T. D. *ChemSusChem* **2011**, *4*, 1566−1569. (e) Gerken, J. B.; McAlpin, J. G.; Chen, J. Y. C.; Rigsby, M. L.; Casey, W. H.; Britt, R. D.; Stahl, S. S. *J. Am. Chem. Soc.* **2011**, *133*, 14431−14442. (f) Zhang, M.; de Respinis, M.; Frei, H. *Nat. Chem.* **2014**, *6*, 362−367.

(6) Kanan, M. W.; Nocera, D. G. *Science* **2008**, *321*, 1072−1075.

(7) Wohler, L.; Witzmann, W. Z. *Anorg. Chem.* **1908**, *57*, 323−352.

(8) The reason we obtained TOF at this potential (1.3 V vs Ag/AgCl) is because the TOF values to be compared were also obtained at this potential.

(9) (a) Chen, G.; Delafuente, D. A.; Sarangapani, S.; Mallouk, T. E. *Catal. Today* **2001**, *67*, 341−355. (b) Gileadi, E. *Electrode Kinetics for Chemists, Chemical Engineers, and Materials Scientists*; Wiley-VCH: New York, 1993; pp 101−184.

(10) (a) Kanan, M. W.; Yano, J.; Surendranath, Y.; Dincă, M.; Yachandra, V. K.; Nocera, D. G. *J. Am. Chem. Soc.* **2010**, *132*, 13692−13701. (b) Surendranath, Y.; Kanan, M. W.; Nocera, D. G. *J. Am. Chem. Soc.* **2010**, *132*, 16501−16509. (c) McAlpin, J. G.; Surendranath, Y.; Dinca, M.; Stich, T. A.; Stoian, S. A.; Casey, W. H.; Nocera, D. G.; Britt, R. D. *J. Am. Chem. Soc.* **2010**, *132*, 6882−6883. (d) Risch, M.; Khare, V.; Zaharieva, I.; Gerencser, L.; Chernev, P.; Dau, H. *J. Am. Chem. Soc.* **2009**, *131*, 6936−6937. (e) Risch, M.; Klingan, K.; Ringleb, F.; Chernev, P.; Zaharieva, I.; Fischer, A.; Dau, H. *ChemSusChem* **2012**, *5*, 542−549.

(11) Junge, H.; Marquet, N.; Kammer, A.; Denurra, S.; Bauer, M.; Wohlrab, S.; Gärtner, F.; Pohl, M.-M.; Spannenberg, A.; Gladiali, S.; Beller, M. *Chem. - Eur. J.* **2012**, *18*, 12749−12758.

(12) (a) Mo, Y.; Stefan, I. C.; Cai, W.-B.; Dong, J.; Carey, P.; Scherson, D. A. *J. Phys. Chem. B* **2002**, *106*, 3681−3686. (b) Hillman, A. R.; Skopek, M. A.; Gurman, S. J. *Phys. Chem. Chem. Phys.* **2011**, *13*, 5252−5263.

(13) Totir, D.; Mo, Y.; Kim, S.; Antonio, M. R.; Scherson, D. A. *J. Electrochem. Soc.* **2000**, *147*, 4594−4597.

(14) Dau, H.; Limberg, C.; Reier, T.; Risch, M.; Roggan, S.; Strasser, P. *ChemCatChem* **2010**, *2*, 724−761.

(15) Bockris, J. O.; Otagawa, T. *J. Phys. Chem.* **1983**, *87*, 2960−2971.

(16) (a) Willems, H.; Kobussen, A. G. C.; DE Wit, J. H. W.; Broers, G. H. J. *J. Electroanal. Chem. Interfacial Electrochem.* **1984**, *170*, 227−242. (b) Yeo, B. S.; Bell, A. T. *J. Am. Chem. Soc.* **2011**, *133*, 5587−5593. (c) Sanchez Casalongue, H. G. S.; Ng, M. L.; Kaya, S.; Friebel, D.; Ogasawara, H.; Nilsson, A. *Angew. Chem.* **2014**, *126*, 7297−7300.